Matter

CellPress

Article

Colloidal quantum dot photodetectors with 10-ns response time and 80% quantum efficiency at 1,550 nm

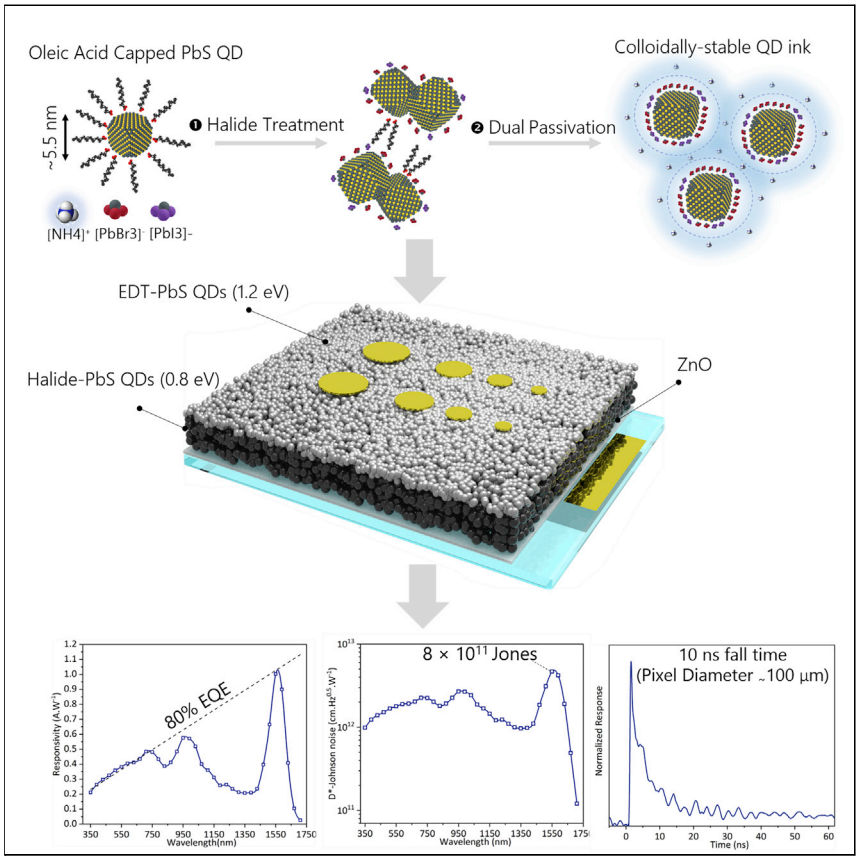

Photodetectors operating in the short-wave IR range (SWIR) are needed for emerging three-dimensional vision applications. Solution-processed semiconductors offer tunable absorption into the SWIR and low-cost fabrication comparing to the epitaxially grown semiconductors. In this study, we present an efficient route to process large colloidal quantum dots with band gap of 0.8 eV into high-quality solids with exceptional optoelectronic properties. The fabricated SWIR photodiodes exhibit a record external quantum efficiency and reasonable detectivity at 1,550 nm as well as a fast response time.

Maral Vafaie, James Z. Fan, Amin Morteza Najarian, ..., Bin Sun, F. Pelayo García de Arquer, Edward H. Sargent

ted.sargent@utoronto.ca

Highlights

An efficient ligand exchange tailored to large PbS CQDs having band gap of 0.8 eV

A stable colloidal quantum dot system with improved passivation and carrier transport

SWIR photodetectors featuring high sensitivity and fast response time at 1,550 nm

Operating stability over 12 h of continuous operation under ambient air

Vafaie et al., Matter 4, 1–12
March 3, 2021
https://doi.org/10.1016/j.matt.2020.12.017

Please cite this article in press as: Vafaie et al., Colloidal quantum dot photodetectors with 10-ns response time and 80% quantum efficiency at 1,550 nm, Matter (2020), https://doi.org/10.1016/j.matt.2020.12.017

Matter

CellPress

Article

Colloidal quantum dot photodetectors with 10-ns response time and 80% quantum efficiency at 1,550 nm

Maral Vafaie,[1] James Z. Fan,[1] Amin Morteza Najarian,[1] Olivier Ouellette,[2] Laxmi Kishore Sagar,[1] Koen Bertens,[1] Bin Sun,[1] F. Pelayo García de Arquer,[1] and Edward H. Sargent[1,*]

Summary

Fast and sensitive infrared (IR) photodetection is of interest for depth imaging that is fundamental to machine vision, augmented reality, and autonomous driving. Colloidal quantum dots (CQDs) are appealing candidates for this goal: in contrast with III–V semiconductors, they offer facile tuning of IR absorption and enable ease of integration via solution processing. So far, the best short-wave IR CQD photodetectors have been limited to 70-ns response time and quantum efficiency of 17% at 1,450 nm. To advance the field using CQDs, large-diameter CQDs are needed that combine passivation with efficient charge transport. Here, we report an efficient ligand-exchange route that tailors the halide passivants and introduces an added exchange step crucial to efficient passivation, removal of unwanted organics, and charge transport. In devices, the CQD solids give rise to external quantum efficiency greater than 80% at 1,550 nm, a measured detectivity of 8 × 10^{11} Jones, and a 10-ns response time.

Introduction

The detection of short-wavelength infrared (SWIR) light is central to optical communications, spectroscopy, biological sensing, surveillance, and environmental mapping. Emerging applications in depth imaging—3D vision for gesture recognition in virtual/augmented reality as well as LiDAR (Light Detection And Ranging) for autonomous driving[1–3]—rely on the accurate temporal detection of short light pulses. This demands fast and efficient photodetection. SWIR operation (e.g., 1,380 and 1,550 nm) offers benefits such as improved eye safety (i.e., higher permitted peak powers) and the increased transmission of particular wavelengths of SWIR light through certain biological materials and atmospheric conditions.[4,5]

Existing solutions for SWIR sensing rely on epitaxially grown semiconductors such as InGaAs and Ge; however, this elevates their cost and militates against their integration on consumer-grade silicon.[6,7] Solution-processed semiconductors, on the other hand, offer tunable absorption into the SWIR and low-temperature fabrication compatible with a range of substrates.[8]

Colloidal quantum dots (CQDs) are inorganic nanocrystals which, when their radii are reduced to about less than twice the size of their exciton Bohr radius (i.e., ~18 nm for PbS), feature band-gap tuning through dot size, including into the SWIR.[8] Their SWIR absorption coefficient benefits from an exponential dependence on dot size,[9] which is especially beneficial relative to organics because the latter

Progress and potential

The realization of fast and sensitive infrared (IR) photodetectors is of interest for three-dimensional vision applications spanning consumer electronics, augmented reality, machine vision, and autonomous driving. Colloidal quantum dots (CQDs) are appealing toward this end: they unite IR-tunable absorption with ease of fabrication. To date, CQD photodetectors operating in the short-wave IR have failed to provide the combination of high responsivity, detectivity, and fast temporal response. To advance this field, large-diameter CQDs are needed that combine passivation with efficient charge transport.

Here, we present an efficient ligand-exchange strategy tailored to large CQDs having a band gap of 0.8 eV. The new well-passivated stable colloidal quantum dots enable high-quality CQD photoactive layers with exceptional optoelectronic properties. As a result, short-wavelength IR photodetectors operating at 1,550 nm with a record external quantum efficiency, reasonable detectivity, and fast response time are demonstrated.

Please cite this article in press as: Vafaie et al., Colloidal quantum dot photodetectors with 10-ns response time and 80% quantum efficiency at 1,550 nm, Matter (2020), https://doi.org/10.1016/j.matt.2020.12.017

exhibit weak absorption at wavelengths longer than 1,300 nm.[10] CQD solids are now available that have compelling optoelectronic properties, including charge transport.[11]

In 2009 Clifford et al.[5] reported CQD photodetectors at 1,450 nm with calculated detectivity of 10^{12} Jones and 70 ns time response. However, the devices delivered quantum efficiencies that were limited to 17%. The use of organic molecules as passivants provided incomplete surface passivation,[11,12] impeding electronic coupling of CQDs and increasing trap-state density.

Halide passivants introduced via a liquid phase exchange have accelerated progress in CQD photovoltaics.[12,13] Unfortunately, the translation of this approach to larger-diameter CQDs has so far failed, since the surface configuration of CQDs changes as the function of dot size: the resultant underpassivated surfaces lead to CQD aggregation and even fusion. This impairs colloidal stability and causes energetic disorder that precludes fast and sensitive photodetection at these wavelengths.

Here, we report CQD photodiodes operating at SWIR wavelengths and featuring high responsivity united with fast response. We tailored bromine content and introduced an additional passivation step, and these strategies enabled CQDs with band gap of 0.8 eV to remain well dispersed and well passivated and to generate CQD solids with an efficient electronic coupling and smooth energy landscape. The stabilized colloidal inks enable an external quantum efficiency (EQE) of 80%, a measured specific detectivity (D^*) of 8×10^{11}, and a time response of 10 ns.

Results and discussion

We started from known ligand exchanges used for PbS quantum dots (QDs) with higher band gaps, i.e., >1 eV, dot diameter <3.5 nm. These involve the exchange of oleic acid-capped QDs to a mixture of halide salts having a low level of lead bromide (we term the exchange LLB) to iodide content (1:5 Br^-/I^-), whereby the newly exchanged dots phase-exchange to, and disperse well in, a polar solvent. Subsequent precipitation and isolation of the dried halide-capped dots allow for the redispersion into a colloidal ink that can then be directly cast, via spin-coating, onto a substrate.[14]

We found that translating this exchange strategy for QDs with larger diameter fails: the final ink results as an unstable, agglomerated mixture with leftover organic content. The best-performing previously reported CQD photodiodes with a band gap in the 1,500 nm and longer range are either limited to layer-by-layer solid exchange procedures with EQEs lower than 60%[15] or achieve high EQE by relying on micron-thick active layers,[16] which would require an applied potential to accelerate charge extraction, thus increasing dark current and compromising overall sensitivity.

As the CQD diameter increases beyond 4 nm, the dot morphology undergoes a transition from octahedron to cuboctahedron: the (100) becomes the dominant facet on the CQD surface (Figure S1).[17] We find that previously reported ligand exchanges fail to passivate the charge-neutral (100) facets, making the resultant inks colloidally unstable in polar solvents, leading to macroscopic aggregates of CQDs (Figure S2) surrounded by organic residue. This makes the final CQD solid prone to irreversible oxidation and favors inhomogeneous fusion between adjacent dots via these unpassivated facets (Figure 1A).[18,19] The loss of quantum confinement within the fused regions gives rise to heterogeneous energy landscapes, and these disrupt the transport of the carriers.[20–22] Additionally, this leads to accumulation of unwanted

[1]Department of Electrical and Computer Engineering, University of Toronto, 10 King's College Road, Toronto, ON M5S 3G4, Canada

[2]Laboratory for Photonics and Interfaces, École Polytechnique Fédérale de Lausanne, Lausanne 1015, Switzerland

*Correspondence: ted.sargent@utoronto.ca

https://doi.org/10.1016/j.matt.2020.12.017

Please cite this article in press as: Vafaie et al., Colloidal quantum dot photodetectors with 10-ns response time and 80% quantum efficiency at 1,550 nm, Matter (2020), https://doi.org/10.1016/j.matt.2020.12.017

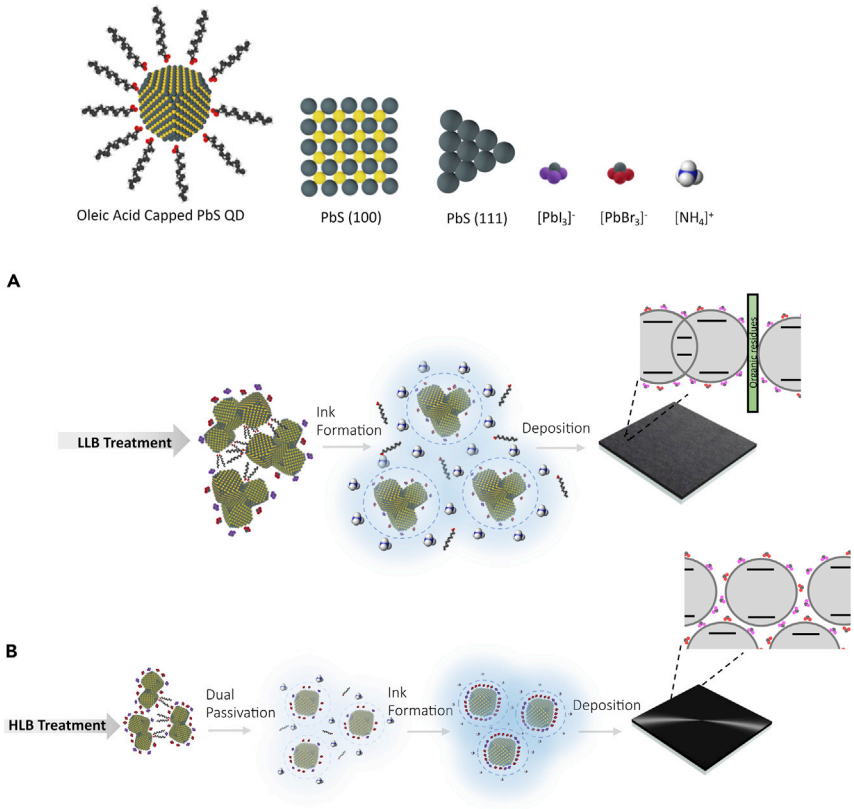

Figure 1. Ligand exchanges: previous strategies compared with the approach investigated herein

(A) Prior reports began with mixed halide treatments with a low level of lead bromide—herein termed the LLB treatment—but we find that it does not efficiently passivate the (100) facets and therefore leads to dot fusion. In making an ink, redispersion is in amines. The result is an inhomogeneous film with an inconsistent energetic landscape.

(B) Here we focus on a higher lead bromide content—termed the HLB treatment—and find that it leads to increased passivation of (100) facets and less agglomeration. A second passivation step is implemented by redispersion in a lower-concentration halide solution, after which final redispersion is done in an amine solvent. This results in a well-passivated stable colloidal ink that delivers a smooth film with improved photophysical properties.

organics that preclude charge transport and impedes the access of halide ligands to unpassivated surface sites.[19]

We therefore sought a new route to SWIR inks for high-quality films (Figure 1B). We first increased the ratio of $PbBr_2$ to PbI_2 (2:5 Br^-/I^-) (high level bromine [HLB] treatment) to provide the (100) surface of the dots with more efficient passivation. PbI_2 has been previously reported to be the dominant passivating ligand for the (111) surface;[13] however, it has less affinity toward the (100) surface.[14] Smaller lead halides have been reported to reduce surface defects on the Pb (100) surface:[23,24] $PbBr_2$ ligands provide the highest surface coverage yields in a mixed halide system for larger PbS QDs and, at the same time, provide sufficient passivation without hindering carrier charge transport in the CQD solid.[14] However, this single step fails to render the CQD ink stable, as there are still some unpassivated fused facets left that provoke agglomerate formation and accumulation of the unwanted organic species.

Please cite this article in press as: Vafaie et al., Colloidal quantum dot photodetectors with 10-ns response time and 80% quantum efficiency at 1,550 nm, Matter (2020), https://doi.org/10.1016/j.matt.2020.12.017

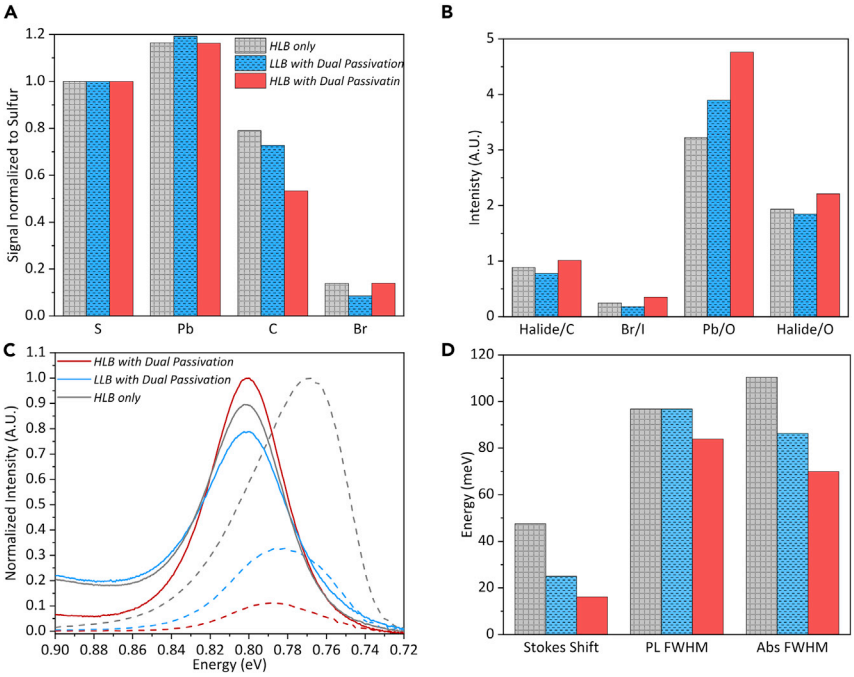

Figure 2. Materials characterization for HLB with dual passivation exchange route versus controls

(A) X-Ray photoelectron spectroscopy (XPS) ratios of the S 2p, Pb 4f, C 1s, and Br 3d of the passivated films normalized to integrated S 2p signal.

(B) XPS ratios of halide (Br 3d and I 3d) to C 1s, Br 3d to I 3d, Pb 4f to O 1s, and halide to O 1s for all passivated films.

(C and D) (C) Normalized absorbance (solid lines) and photoluminescence spectra (dotted lines) of the exchanged films, and (D) their correspondence values for Stokes shift, PL, and absorbance full width at half maximum (FWHM).

Based on these findings, we sought to introduce an additional passivation step immediately after initial precipitation of the dots: we redispersed the CQD precipitate in a diluted mixture of $PbBr_2$ and PbI_2 followed by the addition of butylamine as a stabilizing agent.[25] This second precipitation step keeps the dots separated while the additional halides approach the sites that were out of reach in the precipitation step due to dot fusion/agglomeration. Additionally, this step leads to the efficient removal of unwanted remaining organics. As a result, we achieve a more homogeneous energy landscape, and a colloidally stable ink is obtained that we later deposit to form a smooth film with enhanced photophysical properties.

To assess the impact of each introduced step on the optoelectronic properties of the films, we fabricated two sets of control samples: these controls received the benefit of the modified halide exchange or the additional passivation, but not both. The samples italicized as *HLB only* refer to the set whose exchange pathway was only adjusted by using higher lead bromide. Similarly, the samples italicized as *LLB with dual passivation* denote CQDs that underwent LLB but received the benefit of the additional passivation step. Figure 2 reports X-ray photoelectron spectroscopy (XPS), absorbance, and photoluminescence (PL) studies of control films compared with those prepared using the optimized exchange route (*HLB with dual passivation*). The XPS results reveal that both *HLB only* and *LLB with dual passivation* films suffer from the higher level of organic residue, as well as of oxidized species, indicated by more intense carbon peak in Figure 2A and a lower lead to oxygen peak in Figure 2B. In contrast, higher halide-to-carbon and halide-to-oxygen ratios

Please cite this article in press as: Vafaie et al., Colloidal quantum dot photodetectors with 10-ns response time and 80% quantum efficiency at 1,550 nm, Matter (2020), https://doi.org/10.1016/j.matt.2020.12.017

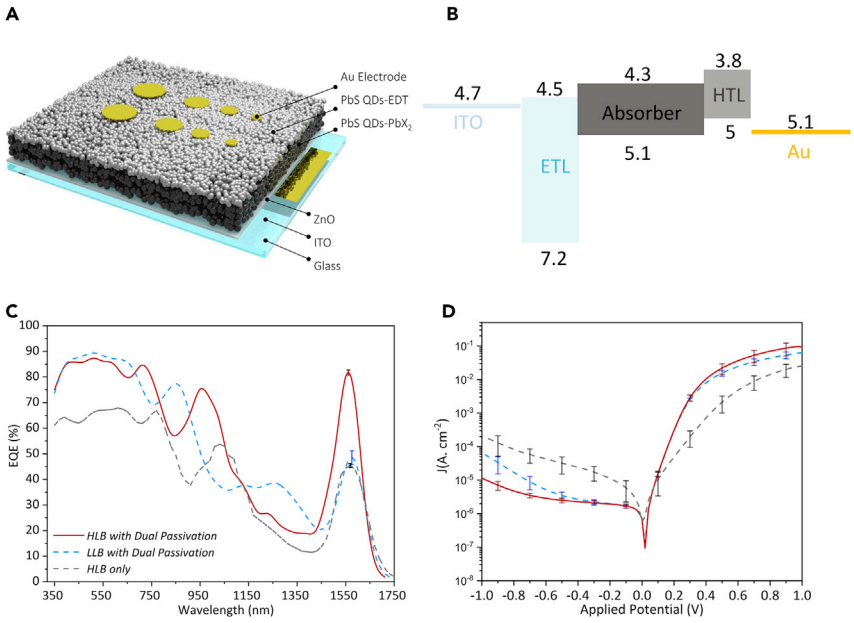

Figure 3. Device structure, energy band diagrams, and performance comparison between the devices with our proposed method and controls

(A) Architecture and (B) band diagrams, (C) EQE spectra of the devices (error bars indicate the standard deviation at the exciton peak), and (D) current density versus voltage behavior under dark conditions for devices with our proposed exchange route versus controls. The error bars are based on standard deviation with minimum sample size of 10. Device area, 0.1 cm^2.

are seen in *HLB with dual passivation* (Figure 2B). This indicates more efficient removal of organics and of oxidative species, and more successful halide passivation. The higher bromine-to-iodine ratio for these films indicates the presence of extra bromine in the system after exchange and highlights its active role in better passivation. Figure 2C shows strong quenching of PL intensity for *HLB with dual passivation*, suggesting increased QD coupling and more efficient carrier transport in the absence of excess organics. Simultaneously, the minimized Stokes shift and PL/absorbance full width at half maximum in Figure 2D indicate improved monodispersity and reduced aggregation of QDs in the solid phase for these samples.[14,26]

Additionally, Fourier transform infrared absorption spectra (Figure S3) show the effective removal of oleic acid ligands by the extra passivation step. The characteristic signals of remaining oleic acid ligands at 2,922 and 2,852 cm^{-1} (the C–H vibrations), and between 1,250 and 1,650 cm^{-1} (COO^- vibrations) are significantly diminished for the *HLB with dual passivation* film.[27,28]

Photodiode devices were fabricated according to the planar device architecture in Figure 3A: a photoactive layer CQDs with 0.8-eV band gap exchanged via the proposed routes, denoted as PbS QDs-PbX_2, sandwiched between a zinc oxide layer as the electron transport material and a thin layer of EDT-treated PbS CQDs with larger band gap as the hole-transport component. The energy level diagram of the representative device is shown in Figure 3B. Figures 3C and 3D compare the results of EQE and dark current density-potential (*J-V*), and Figure S4 studies *J-V* characteristics under illumination for control devices with those treated by *HLB with dual passivation* steps. We find that the optimized exchange route results in well-electronically coupled solids with >74% higher EQE at 1,550 nm exciton peak, >44% lower

Please cite this article in press as: Vafaie et al., Colloidal quantum dot photodetectors with 10-ns response time and 80% quantum efficiency at 1,550 nm, Matter (2020), https://doi.org/10.1016/j.matt.2020.12.017

saturation current at reverse bias in the dark, and >5% higher open-circuit potential and >6% fill factor under illumination (Table S1). A lower amount of bromide anions in the exchange exposes the sensitive (100) surface of the dots to fusion and oxidation, leading to a variable energy landscape, hence ~7% lower open-circuit potential for *LLB with dual passivation* devices. These performance data are collected from each set of devices at their optimal condition: for example, in the case of *HLB with dual passivation*, this occurred at a photoactive layer thickness of 420 nm, a finding explained using Fabry-Perot modeling[29] (Figure S5).

Capacitance-voltage spectroscopy provides insights into the origin of improved performance ("Capacitance-voltage spectroscopy" in Supplemental information; Figures S6 and S7; Table S2). A larger built-in potential (V_{bi}) and longer depletion width (W) for the devices employing dual-exchanged CQD solids compared with *HLB only* suggests the importance of the charge-carrier drift component in achieving efficient collection (Table S2). On the other hand, the doping profile and depletion width of the optimized *HLB dual* and *LLB dual* devices are similar. These results, combined with the observed increased EQE and decreased dark current of *HLB dual* versus *LLB dual*, is indicative of improved diffusion length in *HLB dual* CQD solids. We attribute this to increased mobility and improved passivation, in agreement with results obtained from XPS and PL characterization. Prior studies of charge transport in CQD films have shown that the combination of efficient surface passivation and strong dot coupling can generate longer diffusion length.[30]

To quantify photodetection in devices with our proposed exchange route, we report responsivity (R_λ) at each wavelength (Figure 4A). Responsivity reaches 1 A W^{-1} at peak of 1,550 nm. This is comparable with commercial InGaAs photodetectors with 1 A W^{-1} at the same wavelength.[31,32] Based on the obtained values for responsivity and measurement of noise spectra (Figure S8), the detectivity (D^*) is calculated from[33]

$$D* = \frac{(A.\Delta f)^{1/2} \times R_\lambda}{i_n}, \qquad \text{(Equation 1)}$$

where i_n represents the noise current, A is the electric active area of the photodiode (~0.1 cm^2), and Δf is the electrical bandwidth over which the noise is measured (1 Hz). The D^* as a function of wavelength in Figure 4B demonstrates 8×10^{11} Jones at 1,550 nm.

Photodetection speed was determined by measuring the transient photocurrent responses and reading the time intervals between 10% and 90% of the maximum photocurrent for different pixel sizes, as presented in Figure 4C. The fastest measured fall time is 10 ns, which is the lowest measured fall time of an SWIR photodetector fabricated by solution-processed materials. The photodetection speed of the control devices as well as a more detailed analysis of the temporal responses versus pixel area are included in "Response time studies" in Supplemental information (Figure S9; Tables S3 and S4). The operating stability of the optimized devices was evaluated over 12 h of continuous operation (Figure S10A). The devices retained 71% of initial photoresponse following 12 h of operation under ambient air (Figure S10B).

To contextualize the performance of the photodetectors, we reviewed prior reports of SWIR solution-processed photodetectors with detection in the range 1.4–1.7 μm (Table 1). Organic molecules show low dark currents but also lower photosensitivity in this spectral range. QDs have previously seen impressive photoresponsivity and

Please cite this article in press as: Vafaie et al., Colloidal quantum dot photodetectors with 10-ns response time and 80% quantum efficiency at 1,550 nm, Matter (2020), https://doi.org/10.1016/j.matt.2020.12.017

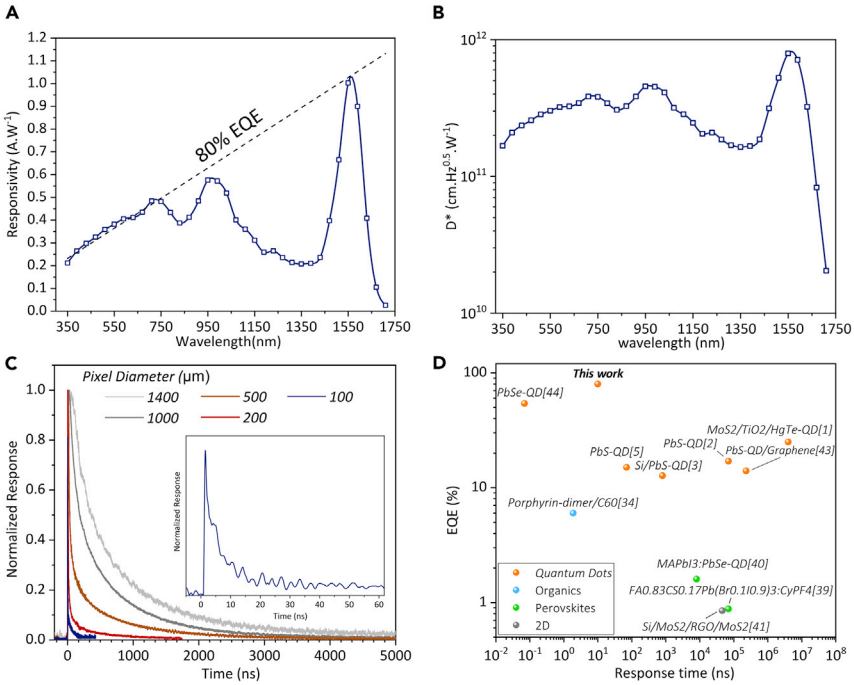

Figure 4. Photodetector characterization

(A–C) (A) Responsivity, (B) specific detectivity spectrum obtained from noise measurement at room temperature at 500 kHz using a signal analyzer, and (C) measured transient photocurrent for different pixel sizes of the detectors fabricated via HLB with dual passivation exchange route. A 150-fs pulsed laser with a 10-kHz repetition rate illuminated each pixel at 850 nm with the average laser fluence of 12 mW cm^{-2}. No external bias was applied to the detector during the measurement. (D) EQE versus response time of the best reported solution-processed photodetectors including this work with detection in the range 1.4–1.7 μm (for more details see Table 1).

detectivity, but prior reports (Figure 4D) left room for the improvements in temporal response reported here.

In summary, we introduce a ligand-exchange strategy that enables high-performing CQD solids with a band gap of 0.8 eV. This approach results in a stable colloidal QD system with improved passivation, a low level of organic residue, and more efficient carrier transport. We report CQD photodetectors having an EQE of 80% at 1,550 nm, a measured detectivity of 8×10^{11} Jones, and a response time of 10 ns.

Experimental procedures

Resource availability

Lead contact

Further information and requests for resources and materials should be directed to and will be fulfilled by Edward H. Sargent, ted.sargent@utoronto.ca.

Materials availability

All unique/stable materials generated in this study are available from the Lead contact.

Data and code availability

Data supporting the findings of this paper are available within the article and its Supplemental information files and from the Lead contact upon reasonable request.

Please cite this article in press as: Vafaie et al., Colloidal quantum dot photodetectors with 10-ns response time and 80% quantum efficiency at 1,550 nm, Matter (2020), https://doi.org/10.1016/j.matt.2020.12.017

Table 1. Photodetection in solution-processed photodetectors in the SWIR range 1.4–1.7 μm

Photoactive material	Photo detector type	λ detection (nm)	Bias (V)	EQE (%)	Responsivity (A W^{-1})	Minimum dark current (A cm^{-2})	Response time			Detectivity (cmHz$^{0.5}$ W^{-1})	Ref.
							Fall time (ns)	Bias (V)	Area (mm^2)		
Porphyrin-dimer/C_{60}	PD	1,400	0	6	0.07[a]	1×10^{-5}	1.87	1	–	2×10^{10}	Zimmerman et al.[35]
PDT:$PC_{61}BM$	PD	1,400	0.1	–	1.5×10^{-3}	1.4×10^{-10}	–	–	–	1×10^{11}	Han et al.[36]
P3:$PC_{71}BM$	PD	1,500	0	0.08	–	1×10^{-6}	–	–	–	2×10^{10}	London et al.[37]
P1:$PC_{61}BM$	PD	1,400	2	0.1	0.01	5×10^{-11}	–	–	–	3×10^{9}	Han et al.[38]
PBBTPD: Tri-$PC_{61}BM$	PD	1,500	0.5	13.4	0.00014	1×10^{-7}	–	–	–	2.2×10^{11}	Zheng et al.[39]
PVK:$CyPF_4$	PD	1,400	0	0.88[a]	0.01	5×10^{-6}	7×10^{4}		10	2×10^{7}	Lin et al.[40]
$MAPbI_3$: PbSe-QD	PD	1,500	1	1.6	0.019	8.3×10^{-7}	8×10^{3}	0	4.5	1.1×10^{11}	Zhang[41]
Si/MoS_2/ RGO/MoS_2	PD	1,550	0	0.85	0.0106	6.4×10^{-3}	46×10^{3}	0	12.56	1.83×10^{12}	Xiao et al.[42]
PbS-QD	PD	1,450	0	15	0.199	1×10^{-7}	70	5	1.96	1×10^{12}[a]	Clifford et al.[5]
PbS-QD	PD	1,550	0	8	0.1	2×10^{-8}	–	–	–	5×10^{12}[a]	Klem et al.[43]
PbS-QD/ graphene	PT	1,600	0.3	14	–	1×10^{-6}	2×10^{5}	0.3	0.0001	4×10^{12}[b]	Nikitskiy et al.[44]
PbSe-QD	PC	800	1.2	54	0.36	1.15×10^{2}	0.07	1.3	0.0001	5.93×10^{7}[a]	Gao et al.[45]
MoS_2/TiO_2/ HgTe-QD	PT	1,500	15	25[a]	0.3	5×10^{-4}	4×10^{6}	1	2×10^{-5}	3×10^{11}[b]	Huo et al.[1]
PbS-QD	PD	1,650	2	17	0.2	2×10^{-8}	7×10^{4}	–	–	6×10^{10}[a]	Dong et al.[2]
PbSe-QD	PD	1,400	1	–	10	1×10^{-9}	4×10^{5}	0	4.5	1×10^{12}[a]	Zhu et al.[46]
Si/PbS-QD	PD	1,490	0.25	12.7	0.153	2×10^{-7}	800	0	5	2.94×10^{11}[a]	Xiao et al.[3]
PbS-QD	**PD**	**1,550**	**0**	**80**[c]	**1**	**1.4×10^{-7}**[d]	**10**	**0**	**0.0078**	**8×10^{11}**[e]	**this work**

Materials are categorized into organic molecules, organohalide metal perovskites, two-dimensional inorganic materials, and inorganic quantum dots. The last row of the table is displayed in boldface to highlight the figure of merits of this work's optimized photodetectors.

[a]Calculated.

[b]Measured.

[c]Relative standard deviation for this parameter is ±3%.

[d]Relative standard deviation for this parameter is ±17%.

[e]Relative standard deviation for this parameter is ±10%.

Synthesis of PbS QDs

Two different sizes of oleic acid-capped nanocrystals were considered for this work, including the larger as the photoabsorber layer with exciton peak targeted at around 1,550 nm and the smaller one as the hole transport layer with the exciton peak at around 1,050 nm. Both of the dot batches were synthesized using the typical Hines synthesis method[34] using modified amounts of PbO and bis(trimethylsilyl) sulfide as Pb and S precursors.

Ligand-exchange pathways

The classic passivation route was started by preparing classic exchange solution known as LLB via dissolving 345 mg of PbI_2 (99.999%, Alfa Aesar), 55 mg of $PbBr_2$ (98%, Sigma-Aldrich), and 27 mg of NaOAc (99.999%, Sigma-Aldrich) in 7.5 mL of *N*,*N*-dimethylformamide (DMF; anhydrous, 98%, Sigma-Aldrich) in a 50-mL centrifuge tube. A diluted solution of OA-PbS in octane (98%, Alfa Aesar) at a concentration of 1.625 mg mL^{-1} was then added to the exchange solution. The tube was vigorously shaken for 30 s to facilitate dot transfer to the DMF phase. Subsequently, the tube was centrifuged at 7,830 rpm for 30 s and the octane phase was discarded. After the main exchange step, the remaining solution was washed three times with octane, with a similar centrifuge step in between each washing step. After the final wash, 2.5 mL of toluene (distilled in glass, Caledon) was added gradually and then

Please cite this article in press as: Vafaie et al., Colloidal quantum dot photodetectors with 10-ns response time and 80% quantum efficiency at 1,550 nm, Matter (2020), https://doi.org/10.1016/j.matt.2020.12.017

centrifuged for 120 s to precipitate the QDs. The supernatant was removed and the tube was dried under vacuum for 10 min.

For the optimized exchange route, the modified exchange solution labeled as HLB was made similarly to LLB except that the amount of $PbBr_2$ was increased to 110 mg. The exchange procedure was carried out in the same manner as for the classic route up to the precipitation step. After the third wash, the supernatant was discarded and the precipitated QDs were redispersed in a diluted version of LLB mixture containing 2 mM $PbBr_2$ and 10 mL of PbI_2. Subsequently, a 10-μL volume of 50% (v/v) diluted solution and butan-1-amine (BTA) (99%, Sigma-Aldrich) was added to the tubes to restabilize the colloid. Before vortexing, the CQDs were kept in a sealed glass tube for 2 min and then vortexed to ensure effective dual passivation. Next, 600 μL of toluene was added to precipitate the CQDs and the tubes were centrifuged again for 120 s. A reduced time of 3 min was needed for vacuum-drying the dots, likely due to the effective organic removal using the dual passivation strategy.

The exchanged QDs were dispersed in a solution of 25% DMF and 75% BTA at desired concentrations.

Device fabrication

Indium tin oxide (ITO) glass substrates (Delta Technologies, 80–90 Ω square^{-1}) were cleaned and used as conductive substrates. For the electron transport layer, a ZnO sol-gel solution was prepared by mixing zinc acetate dihydrate (99.999%, Sigma-Aldrich) in anhydrous 2-methoxyethanol (99.8%, Sigma-Aldrich) at a concentration of 260 mM. After vigorous mixing, 2-aminoethan-1-ol (99%, Sigma-Aldrich) at a ratio of 0.28 wt % of zinc acetate dihydrate was added and the mixture was stirred overnight. Thereafter, the prepared solution was spin-coated at 4,000 rpm on substrate and annealed at 210°C for 30 min in a fume hood with controlled temperature and relative humidity of 25°C and 35%, respectively. All the ZnO films were used immediately after preparation or after brief storage in a nitrogen-filled glovebox. The as-prepared ink of CQDs was dynamically spin-coated on the ZnO layer under mild nitrogen pressure. The final films were annealed in a glovebox at 70°C for 15 min and were kept inside the glovebox to cool down before the next step. Next, using the smaller synthesized QDs, a thin layer of ethane-1,2-dithiol (EDT)-treated QDs was deposited on top of the photoactive layer through layer-by-layer deposition to act as hole transporting layer. The exact method for EDT solid-state ligand exchange is described by Fan et al.[14] Finally, a 160-nm layer of Au was deposited by electron beam evaporation as the top metal electrode.

Device and materials characterization

J-V measurements were taken using a sourcemeter (Keithley 2400). For *J-V* measurements under light conditions, 4.9 mm^2 of each pixel was illuminated under simulated AM 1.5G illumination (Sciencetech class A). Devices were measured under continuous nitrogen gas flow.

The responsivity and quantum efficiency of the devices were measured using a QUANTX-300 Newport measurement system. A standard calibrated Si/Ge reference detector (BD005, Newport) was used to provide reliable absolute values of quantum efficiency/responsivity over the wavelength range from 350 to 1,800 nm. The calibration procedure is conducted before each set of measurements to create the reference values. A silicon photovoltaic test cell is used to further validate the calibration procedure.

Please cite this article in press as: Vafaie et al., Colloidal quantum dot photodetectors with 10-ns response time and 80% quantum efficiency at 1,550 nm, Matter (2020), https://doi.org/10.1016/j.matt.2020.12.017

Capacitance-voltage spectra of the photodiodes were acquired with an LCR meter (4284A, Agilent) at frequency of 10 kHz, AC signal of 50 mV, and under dark conditions. Impedance spectroscopy was carried out with the photodetectors connected to an Autolab Potentiostat/Galvanostat module with an applied AC voltage perturbation of 20 mV while the device was kept in dark and short-circuit conditions.

Noise spectra were measured up to 500 kHz using a signal analyzer (N9010A, Agilent) combined with a low-noise transimpedance preamplifier powered by electric batteries. Devices were operated under short-circuit conditions. Noise measurements were carried out in the absence of room illumination at room temperature for the pixels with 0.1-cm^2 area. To determine the resolution limit of the signal analyzer, we recorded another spectrum with no device connected to the instrument. Using the obtained average noise signal at 500 kHz, set bandwidth of 1 Hz, and amplification of 10^7 V A^{-1} from the preamplifier, the noise current density was calculated.

The temporal response of each photodetector was evaluated by measuring transient photocurrent (TPC) recorded with a 1-GHz oscilloscope (DSO8104A Infinium, Agilent) while a 150-fs pulsed laser (PHAROS, Light Conversion) with a 10-kHz repetition rate illuminated each individual photodetector pixel. Each device contained an array of circular pixels with different sizes (diameter in the range of 200–1,400 μm) to study and minimize the contribution of capacitance on response time. No external bias was applied to the detectors during the measurement. All TPC measurements were done at 850 nm with the average laser fluence of 12 mW cm^{-2}. It should be mentioned that we did not observe a change in response time at the illumination of 850 nm and 1,550 nm for pixels with bigger areas. However, there is a technical limitation with our laser source at 1,550 nm as it provides much lower power (more than 5-fold).

The operational stability of photodetectors was assessed using a 940-nm diode laser controlled by a function generator to produce square pulses with frequency and pulse width of 100 Hz and 80 μs, respectively. The transient photoresponse of the devices (pixel size of 0.1 cm^2) was recorded using the 1-GHz oscilloscope (no external bias, 50 Ω impedance) over 12 h of operation under ambient atmosphere. The average power of the laser pulses was maintained at 0.6 mW, which translates to peak irradiances of 750 mW cm^{-2}.

XPS was measured using a Thermo Scientific K-Alpha system for exchanged QDs deposited on ITO substrates. All intensities were normalized to the sulfur signal. Optical absorption measurements were carried out in a Lambda 950500 UV-visible-IR spectrophotometer on exchanged QDs deposited on glass substrates. Photoluminescence measurements were performed with a Horiba Fluorolog Time Correlated Single Photon Counting System equipped with UV/Vis/NIR photomultiplier detectors, dual grating spectrometers, and a monochromatized xenon lamp excitation source. The QD deposited on glass substrate was excited at λ = 550 nm. The UPS measurements were carried out on ZnO, halide passivated, and EDT-treated PbS-QD films on ITO using ESCALAB 250Xi system. A He-Iα lamp ($h\nu$ = 21.22 eV) was used as the radiation source and the samples were kept under −5 V bias during the measurement. Transmission electron microscopy (TEM) samples were prepared by dropping a highly diluted oleic acid-capped CQD solution in octane on a carbon-coated Cu grid. The prepared samples were kept under vacuum overnight and subsequently measured on a Hitachi H3300F. Scanning electron microscopy images were obtained by a Hitachi S-5200 microscope.

Supplemental information

Supplemental information can be found online at https://doi.org/10.1016/j.matt.2020.12.017.

Acknowledgments

The authors would like to thank L. Levina, E. Palmiano, R. Wolowiec, and D. Kopilovic for their technical assistance during this research. This work was supported by the Natural Sciences and Engineering Research Council of Canada Alexander Graham Bell Canada Graduate Scholarships (CGS-D), Materials for Enhanced Energy Technologies scholarships, and the NSERC Collaborative Research and Training Experience program grant number 466083.

Author contributions

M.V., J.Z.F., and A.M.N. conceived the idea. M.V. and A.M.N. designed and directed the study. M.V. fabricated and characterized samples and devices. O.O. did theoretical modeling of exciton peak absorbance. K.B. performed XPS characterizations. L.K.S. provided TEM images. A.M.N. performed noise measurements. A.M.N., B.S., F.P.G.d.A., and E.H.S. provided advice. M.V., F.P.G.d.A., and E.H.S. composed the manuscript. All authors commented on the manuscript and have given approval to the final version of the manuscript.

Declaration of interests

The authors declare no competing interests.

Received: August 2, 2020
Revised: November 16, 2020
Accepted: December 14, 2020
Published: January 8, 2021

References

1. Huo, N., Gupta, S., and Konstantatos, G. (2017). MoS_2-HgTe quantum dot hybrid photodetectors beyond 2 μm. Adv. Mater. *29*, https://doi.org/10.1002/adma.201606576.
2. Dong, C., Liu, S., Barange, N., Lee, J., Pardue, T., Yi, X., Yin, S., and So, F. (2019). Long-wavelength lead sulfide quantum dots sensing up to 2600 nm for short-wavelength infrared photodetectors. ACS Appl. Mater. Interfaces *11*, 44451–44457.
3. Xiao, X., Xu, K., Yin, M., Qiu, Y., Zhou, W., Zheng, L., Cheng, X., Yu, Y., and Ning, Z. (2020). High quality silicon: colloidal quantum dot heterojunction based infrared photodetector. Appl. Phys. Lett. *116*, 101102.
4. Kim, J., Ouellette, O., Voznyy, O., Wei, M., Choi, J., Choi, M.-J., Jo, J.W., Baek, S.-W., Fan, J., Saidaminov, M.I., et al. (2018). Butylamine-catalyzed synthesis of nanocrystal inks enables efficient infrared CQD solar cells. Adv. Mater. *30*, 1803830.
5. Clifford, J.P., Konstantatos, G., Johnston, K.W., Hoogland, S., Levina, L., and Sargent, E.H. (2009). Fast, sensitive and spectrally tuneable colloidal-quantum-dot photodetectors. Nat. Nanotechnol. *4*, 40–44.
6. García de Arquer, F.P., Armin, A., Meredith, P., and Sargent, E.H. (2017). Solution-processed semiconductors for next-generation photodetectors. Nat. Rev. Mater. *2*, 16100.
7. Li, Q., Guo, Y., and Liu, Y. (2019). Exploration of near-infrared organic photodetectors. Chem. Mater. *31*, 6359–6379.
8. Saran, R., and Curry, R.J. (2016). Lead sulphide nanocrystal photodetector technologies. Nat. Photon. *10*, 81–92.
9. Cademartiri, L., Montanari, E., Calestani, G., Migliori, A., Guagliardi, A., and Ozin, G.A. (2006). Size-dependent extinction coefficients of PbS quantum dots. J. Am. Chem. Soc. *128*, 10337–10346.
10. Liu, X., Lin, Y., Liao, Y., Wu, J., and Zheng, Y. (2018). Recent advances in organic near-infrared photodiodes. J. Mater. Chem. C *6*, 3499–3513.
11. Yuan, M., Liu, M., and Sargent, E.H. (2016). Colloidal quantum dot solids for solution-processed solar cells. Nat. Energy *1*, 16016.
12. Carey, G.H., Abdelhady, A.L., Ning, Z., Thon, S.M., Bakr, O.M., and Sargent, E.H. (2015). Colloidal quantum dot solar cells. Chem. Rev. *115*, 12732–12763.
13. Ning, Z., Voznyy, O., Pan, J., Hoogland, S., Adinolfi, V., Xu, J., Li, M., Kirmani, A.R., Sun, J.P., Minor, J., et al. (2014). Air-stable n-type colloidal quantum dot solids. Nat. Mater. *13*, 822–828.
14. Fan, J.Z., Andersen, N.T., Biondi, M., Todorović, P., Sun, B., Ouellette, O., Abed, J., Sagar, L.K., Choi, M.J., Hoogland, S., et al. (2019). Mixed lead halide passivation of quantum dots. Adv. Mater. *31*, 1904304.
15. Bi, Y., Bertran, A., Gupta, S., Ramiro, I., Pradhan, S., Christodoulou, S., Majji, S.N., Akgul, M.Z., and Konstantatos, G. (2019). Solution processed infrared- and thermo-photovoltaics based on 0.7 eV bandgap PbS colloidal quantum dots. Nanoscale *11*, 838–843.
16. Fan, J.Z., Vafaie, M., Bertens, K., Sytnyk, M., Pina, J.M., Sagar, L.K., Ouellette, O., Proppe, A.H., Rasouli, A.S., Gao, Y., et al. (2020). Micron thick colloidal quantum dot solids. Nano Lett. *20*, 5284–5291.
17. Balazs, D.M., Dirin, D.N., Fang, H.H., Protesescu, L., Ten Brink, G.H., Kooi, B.J., Kovalenko, M.V., and Loi, M.A. (2015). Counterion-mediated ligand exchange for PbS colloidal quantum dot superlattices. ACS Nano *9*, 11951–11959.
18. Choi, H., Ko, J.H., Kim, Y.H., and Jeong, S. (2013). Steric-hindrance-driven shape transition

in PbS quantum dots: understanding size-dependent stability. J. Am. Chem. Soc. *135*, 5278–5281.

19. Kim, Y., Che, F., Jo, J.W., Choi, J., García de Arquer, F.P., Voznyy, O., Sun, B., Kim, J., Choi, M.J., Quintero-Bermudez, R., et al. (2019). A facet-specific quantum dot passivation strategy for colloid management and efficient infrared photovoltaics. Adv. Mater. *31*, 1805580.

20. Lan, X., Chen, M., Hudson, M.H., Kamysbayev, V., Wang, Y., Guyot-Sionnest, P., and Talapin, D.V. (2020). Quantum dot solids showing state-resolved band-like transport. Nat. Mater. *19*, 323–330.

21. Liu, M., Voznyy, O., Sabatini, R., García De Arquer, F.P., Munir, R., Balawi, A.H., Lan, X., Fan, F., Walters, G., Kirmani, A.R., et al. (2017). Hybrid organic-inorganic inks flatten the energy landscape in colloidal quantum dot solids. Nat. Mater. *16*, 258–263.

22. Yazdani, N., Andermatt, S., Yarema, M., Farto, V., Bani-Hashemian, M.H., Volk, S., Lin, W.M.M., Yarema, O., Luisier, M., and Wood, V. (2020). Charge transport in semiconductors assembled from nanocrystal quantum dots. Nat. Commun. *11*, 2852.

23. Winslow, S.W., Liu, Y., Swan, J.W., and Tisdale, W.A. (2019). Quantification of a PbCl x shell on the surface of PbS nanocrystals. ACS Mater. Lett. *1*, 209–216.

24. Jung, Y.K., Butler, K.T., and Walsh, A. (2017). Halide perovskite heteroepitaxy: bond formation and carrier confinement at the PbS-CsPbBr3 interface. J. Phys. Chem. C *121*, 27351–27356.

25. Fan, J.Z., Liu, M., Voznyy, O., Sun, B., Levina, L., Quintero-Bermudez, R., Liu, M., Ouellette, O., García De Arquer, F.P., Hoogland, S., et al. (2017). Halide re-shelled quantum dot inks for infrared photovoltaics. ACS Appl. Mater. Interfaces *9*, 37536–37541.

26. Li, X., Zhao, Y.B., Fan, F., Levina, L., Liu, M., Quintero-Bermudez, R., Gong, X., Quan, L.N., Fan, J., Yang, Z., et al. (2018). Bright colloidal quantum dot light-emitting diodes enabled by efficient chlorination. Nat. Photon. *12*, 159–164.

27. Tang, J., Kemp, K.W., Hoogland, S., Jeong, K.S., Liu, H., Levina, L., Furukawa, M., Wang, X., Debnath, R., Cha, D., et al. (2011). Colloidal-quantum-dot photovoltaics using atomic-ligand passivation. Nat. Mater. *10*, 765–771.

28. Ning, Z., Dong, H., Zhang, Q., Voznyy, O., and Sargent, E.H. (2014). Solar cells based on inks of n-type colloidal quantum dots. ACS Nano *8*, 10321–10327.

29. Ouellette, O., Hossain, N., Sutherland, B.R., Kiani, A., García De Arquer, F.P., Tan, H., Chaker, M., Hoogland, S., and Sargent, E.H. (2016). Optical resonance engineering for infrared colloidal quantum dot photovoltaics. ACS Energy Lett. *1*, 852–857.

30. Carey, G.H., Levina, L., Comin, R., Voznyy, O., and Sargent, E.H. (2015). Record charge carrier diffusion length in colloidal quantum dot solids via mutual dot-to-dot surface passivation. Adv. Mater. *27*, 3325–3330.

31. Thorlabs. Photodiodes. https://www.thorlabs.com/newgrouppage9.cfm?objectgroup_id=285.

32. Hamamatsu. InGaAs photodiodes. https://www.hamamatsu.com/us/en/product/optical-sensors/photodiodes/ingaas-photodiode/index.html.

33. Ahmadi, M., Wu, T., and Hu, B. (2017). A review on organic-inorganic halide perovskite photodetectors: device engineering and fundamental physics. Adv. Mater. *29*, https://doi.org/10.1002/adma.201605242.

34. Hines, M.A., and Scholes, G.D. (2003). Colloidal PbS nanocrystals with size-tunable near-infrared emission: observation of post-synthesis self-narrowing of the particle size distribution. Adv. Mater. *15*, 1844–1849.

35. Zimmerman, J.D., Diev, V.V., Hanson, K., Lunt, R.R., Yu, E.K., Thompson, M.E., and Forrest, S.R. (2010). Porphyrin-tpe/C60 organic photodetectors with 6.5% external quantum efficiency in the near infrared. Adv. Mater. *22*, 2780–2783.

36. Han, J., Qi, J., Zheng, X., Wang, Y., Hu, L., Guo, C., Wang, Y., Li, Y., Ma, D., Qiao, W., et al. (2017). Low-bandgap donor-acceptor polymers for photodetectors with photoresponsivity from 300 nm to 1600 nm. J. Mater. Chem. C *5*, 159–165.

37. London, A.E., Huang, L., Zhang, B.A., Oviedo, M.B., Tropp, J., Yao, W., Wu, Z., Wong, B.M., Ng, T.N., and Azoulay, J.D. (2017). Donor-acceptor polymers with tunable infrared photoresponse. Polym. Chem. *8*, 2922–2930.

38. Han, J., Yang, D., Ma, D., Qiao, W., and Wang, Z.Y. (2018). Low-bandgap polymers for high-performance photodiodes with maximal EQE near 1200 nm and broad spectral response from 300 to 1700 nm. Adv. Opt. Mater. *6*, https://doi.org/10.1002/adom.201800038.

39. Zheng, L., Zhu, T., Xu, W., Liu, L., Zheng, J., Gong, X., and Wudl, F. (2018). Solution-processed broadband polymer photodetectors with a spectral response of up to 2.5 μm by a low bandgap donor-acceptor conjugated copolymer. J. Mater. Chem. C *6*, 3634–3641.

40. Lin, Q., Wang, Z., Young, M., Patel, J.B., Milot, R.L., Martinez Maestro, L., Lunt, R.R., Snaith, H.J., Johnston, M.B., and Herz, L.M. (2017). Near-infrared and short-wavelength infrared photodiodes based on dye-perovskite composites. Adv. Funct. Mater. *27*, 1702485.

41. Zhang, B. (2019). Solution-Processed Broadband Bulk Heterojunction Perovskite Photodetectors (University of Akron), MSc Thesis.

42. Xiao, P., Mao, J., Ding, K., Luo, W., Hu, W., Zhang, X., Zhang, X., and Jie, J. (2018). Solution-processed 3D RGO-MoS_2/pyramid Si heterojunction for ultrahigh detectivity and ultra-broadband photodetection. Adv. Mater. *30*, 1801729.

43. Klem, E.J.D., Gregory, C., Temple, D., and Lewis, J. (2015). PbS colloidal quantum dot photodiodes for low-cost SWIR sensing. In Infrared Technology and Applications XLI (Proceedings of SPIE Defense + Security 2015). https://doi.org/10.1117/12.2178532.

44. Nikitskiy, I., Goossens, S., Kufer, D., Lasanta, T., Navickaite, G., Koppens, F.H.L., and Konstantatos, G. (2016). Integrating an electrically active colloidal quantum dot photodiode with a graphene phototransistor. Nat. Commun. *7*, 11954.

45. Gao, J., Nguyen, S.C., Bronstein, N.D., and Alivisatos, A.P. (2016). Solution-processed, high-speed, and high-quantum-efficiency quantum dot infrared photodetectors. ACS Photon. *3*, 1217–1222.

46. Zhu, T., Zheng, L., Yao, X., Liu, L., Huang, F., Cao, Y., and Gong, X. (2019). Ultrasensitive solution-processed broadband PbSe photodetectors through photomultiplication effect. ACS Appl. Mater. Interfaces *11*, 9205–9212.